



# ATLAS NOTE

March 16, 2015



## Re-analysis of the 2012 test-beam data

P. Giromini<sup>a,b</sup>, J. Gonski<sup>a</sup>, T. Lazovich<sup>a</sup>, H. Skottowe<sup>a</sup>

<sup>a</sup>*Harvard University, Cambridge, Massachusetts 02138, USA*

<sup>b</sup>*Laboratori Nazionali di Frascati, Istituto Nazionale di Fisica Nucleare, Frascati, Italy*

### Abstract

We present a re-analysis of the 2012 test-beam data. In these data, we find that the spatial resolution of micromegas equipped with VMM1 electronics is worse than commonly believed. We extend our analysis of 2012 test-beam data by adding a comparison to the findings of the recent note ATL-COM-MUON-2015-001.

## 1 Introduction

In a previous study [1], we have measured the response of one micromega detector built according to the NSW specifications and equipped with the same VMM1 front-end electronics used in the 2012 test-beam campaign. We have measured the spatial coordinate of incident muons with the charge-barycenter (centroid) and the  $\mu$ TPC methods using tracks with different angles of incidence and clusters of different multiplicities.

In the charge-barycenter mode, the  $x$  position of a track is derived as  $x_{\text{clu}} = \sum q_i x_i / \sum q_i$  (mm), where  $q_i$  is the charge collected by the strip at  $x_i$ . If  $z_d = 5$  mm is the drift thickness,  $x_{\text{clu}}$  measures the  $x$  position of a track at  $z_d/2 = 2.5$  mm.

In the  $\mu$ TPC mode, the TDO time (ns) of each strip  $i$  is converted into a coordinate  $z_i = A - TDO_i/B$ , where  $TDO_i$  is the peaktimes (ns) of strip  $i$ ,  $B=20$  ns/mm is the inverse of the drift velocity, and  $A$  is an arbitrary constant. The  $(x_i, z_i)$  points in a cluster are fitted with a straight line  $z = mx + c$ , and the cluster  $x$  position is evaluated as  $x_{\text{tpc}} = (2.5 - c)/m$  (mm). In the fit, the errors of the  $z_i$  coordinate are arbitrarily set to 0.25 mm (or 5 ns). The constant  $A$  is then tuned to yield  $\langle x_{\text{clu}} - x_{\text{tpc}} \rangle = 0$ . Following the fitting procedure of Ref [1], we prune the cluster strips which have a fit residual larger than 4 (or 1 mm). As noted in Ref [1], the idea itself is elegant but does not improve at all the  $x_{\text{tpc}}$  resolution.

In Ref. [1], we show that the RMS deviation of the difference of the two measurements is  $\approx 2$  mm for tracks with angle of incidence  $\approx 23^\circ$ . Since the uncertainty of the centroid cannot be larger than 0.7 mm, that result, referred to as HCRT result in the following, implies that the spatial resolution of the  $\mu$ TPC method is in the ball-park of 2 mm. This resolution is 10 times worse than that, referred to as TB result in the following, obtained analyzing the 2012 test-beam data [2]. Our finding has ruffled a lot of feathers, and there have been suggestions that we did not properly tune the VMM electronics. However, the  $\approx 130 \mu\text{m}$  resolution [2] for  $20^\circ$  tracks is obtained using  $\approx 10\%$  of the collected data. We have therefore re-analyzed these data with the same procedure used in Ref. [1] and using all events.

In Sec. 2, we analyze the PDO and TDO distribution for each channel of the 8 micromegas used in the test beam. We show that the effective VMM thresholds at the test beam are comparable to the HCRT ones. However, since the real TB thresholds were lower, the TB data pay the price of many dead or hot channels. A procedure is found to minimize the impact of noisy channels (we cannot resuscitate dead channels, yet). In Sec. 3, we measure the RMS deviation of the difference of the spatial coordinates measured with the centroid and  $\mu$ TPC methods, and find it totally consistent with the HCRT result. We also present results on the spatial resolution of the centroid and  $\mu$ TPC standalone methods based on all the collected events. We find that the RMS resolution of the centroid method (0.64 mm) is consistent with the NSW TDR expectation (0.5 mm), but that of the  $\mu$ TPC method (1.34 mm) is an order of magnitude worse than what is reported in Ref. [2] (0.11 mm) and incorporated in the NSW TDR [3] (0.1 mm). In Sec. 4, we describe a novel approach to combine the two methods which improves the spatial resolution to 0.5 mm. The gloomy conclusion has been anticipated to this introduction. In Sec. 5, we compare our results to those presented in Ref. [4].

## 2 On the thresholds, PDO and TDO distributions

In the following, we analyze Run 8013 in which muons have a  $30^\circ$  angle of incidence. Each of the 8 micromegas in the beamline (T1 to T8) are equipped with two VMM1 front-end boards reading 128 strips. The data are available at [5] together with the calibration files for each channel. In this run, the thresholds are set at a nominal value of 20 mV, the neighbor-enable option is off, the PDO scale is 9 mV/fC, the TAC scale is 500 ns, the peaktimes is 50 ns, and the mesh voltage is 540 V.

In Run 8013, the PDO and TDO values are digitized 8 times to reduce the uncertainty from 3 to 2.5 mV. Although they were neglected in [2], voltage-leakage corrections are not negligible, and we

Table 1: Number of events with at least one strip or one cluster in the fiducial region for each micromega.

Micromega	$\geq 1$ strip	$\geq 1$ cluster
T3	7490	6181
T4	13600	11315
T5	7108	6006
T6	13413	11260
T7	7796	6543
T8	13917	11719

apply them as specified in Ref. [6].

The HCRT results in [1] are obtained using a mesh voltage of 550 V and a shaping time of 100 ns, and therefore the strip signals are a factor of two larger than those in Run 8013. As shown by Fig. 1, which should be compared with Fig. 9 of [1], the effective thresholds (fC) in Run 8013 are indeed slightly higher than the HCRT ones because the HCRT gain is a factor of two higher. However, the lower test-beam thresholds (mV) cause the presence of many dead or noisy PDO and TDO channels. TDO distributions are shown in Fig. 2, which should be compared with Fig. 10 of [1]. One also notes that the TDO distributions are not centered in the TAC range, but are truncated at the TAC-scale maximum value. This can explain why the ART-signal time-width measured at the test beam [2] is 3 – 4 times shorter than that measured at the HCRT [6].

One of the VMM chips in T1 is broken, and one in T2 failed calibrations because of the noise. We will not consider these chambers in the following. To reduce the electronic noise, we apply an offline PDO-threshold cut of 1.0, 1.0, 1.0, 1.5, 4.0, and 3.0 fC to the PDO values of T3, T4, T5, T6, T7, and T8, respectively. We also require strips to have TDO values larger than 360 ns and smaller than 520 ns. The result of this cut is shown in Fig. 3.

### 3 Micromega performance

We reconstruct clusters using the *pacman* algorithm described in Ref. [1]. We apply a fiducial cut excluding clusters with centroid in the first and last 8 strips of each chamber. Run 8013 consists of 18290 events; Table 1 lists the number of events with at least one strip in a chamber and the number of events with at least a reconstructed cluster in the fiducial region. The position  $x_{\text{clu}}$  is reconstructed for all clusters, whereas  $x_{\text{tpc}}$  is reconstructed only for clusters with multiplicity equal or larger than three. When reconstructing  $x_{\text{tpc}}$ , we use the strips in a cluster with a distance from  $x_{\text{clu}}$  equal or smaller than 2 mm (never use more than 10 strips). The fraction of events with a double cluster is 4% higher than in Ref. [1], because the front-end electronics is more noisy. The fraction of clusters with one hole is 41%, four times higher than in Ref. [1] because of the many dead channels. The fraction of clusters with 2 holes is 1.4%.

The multiplicity distributions of the reconstructed clusters is shown in Fig. 4. The average multiplicity is  $\simeq 4.8$  for tracks with  $30^\circ$  angle of incidence whereas 7-8 strips with a signal were expected. The average multiplicity is comparable to the one measured in Ref. [1] for  $23^\circ$  tracks because the test-beam data have a lot of dead VMM1 channels. When comparing cluster positions in different chambers, we always limit the distance of their centroids to  $\pm 3$  mm to remove accidental clusters. The micromega efficiency is measured by selecting events with a cluster in T3 and T8 and counting the number of times a cluster is also found in chamber T4 (or T5, or T6, or T7). The average micromega efficiency for tracks with a  $30^\circ$  angle of incidence is  $\simeq 95\%$ .

The different chambers have been aligned in the following way. We construct the distributions  $x_{\text{clu}}^{T8} -$

Not reviewed, for internal circulation only

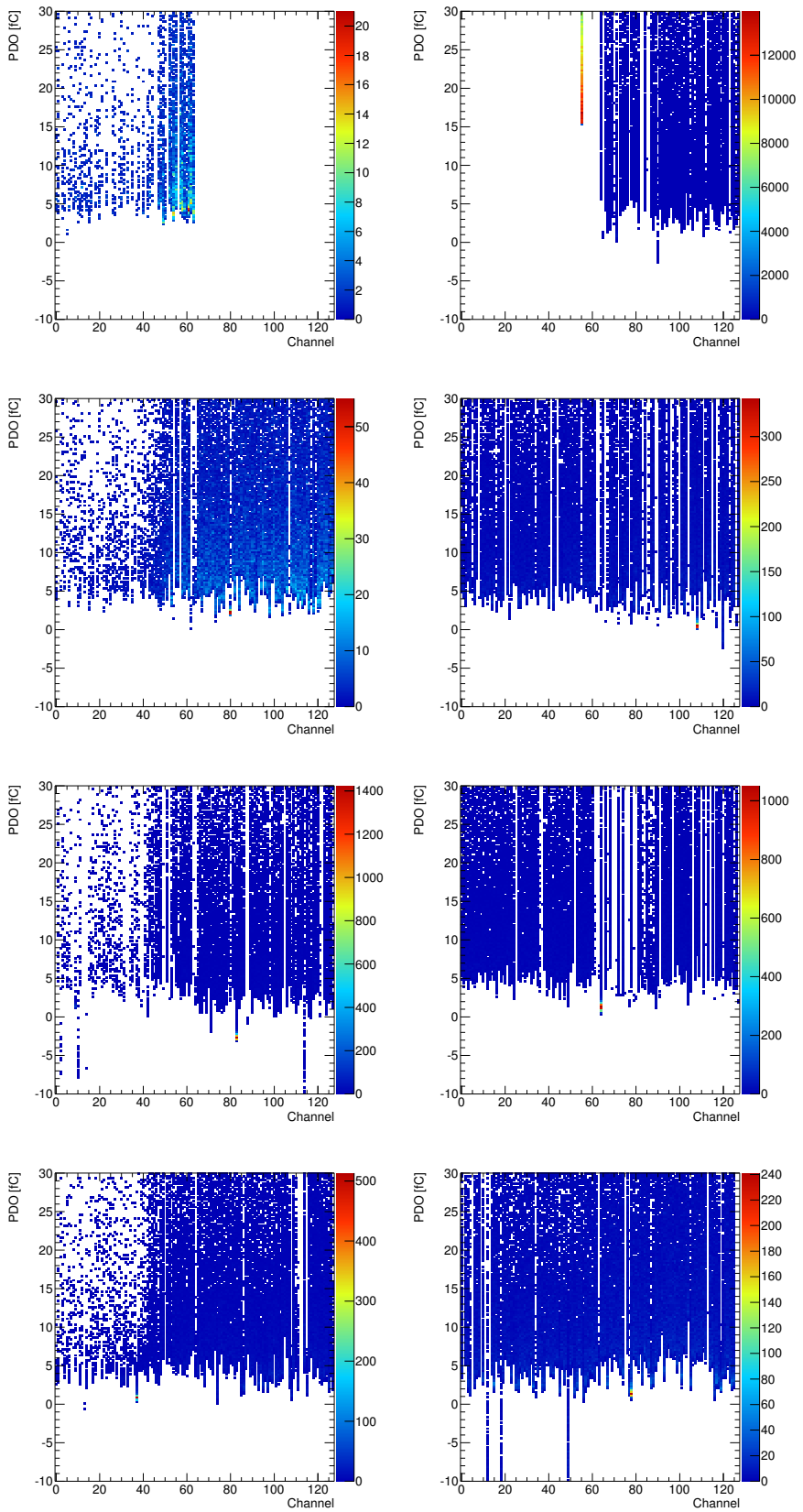


Figure 1: Charge deposited in each channel in Run 8013. This figure is analogous to Fig. 9 of [1].

Not reviewed, for internal circulation only

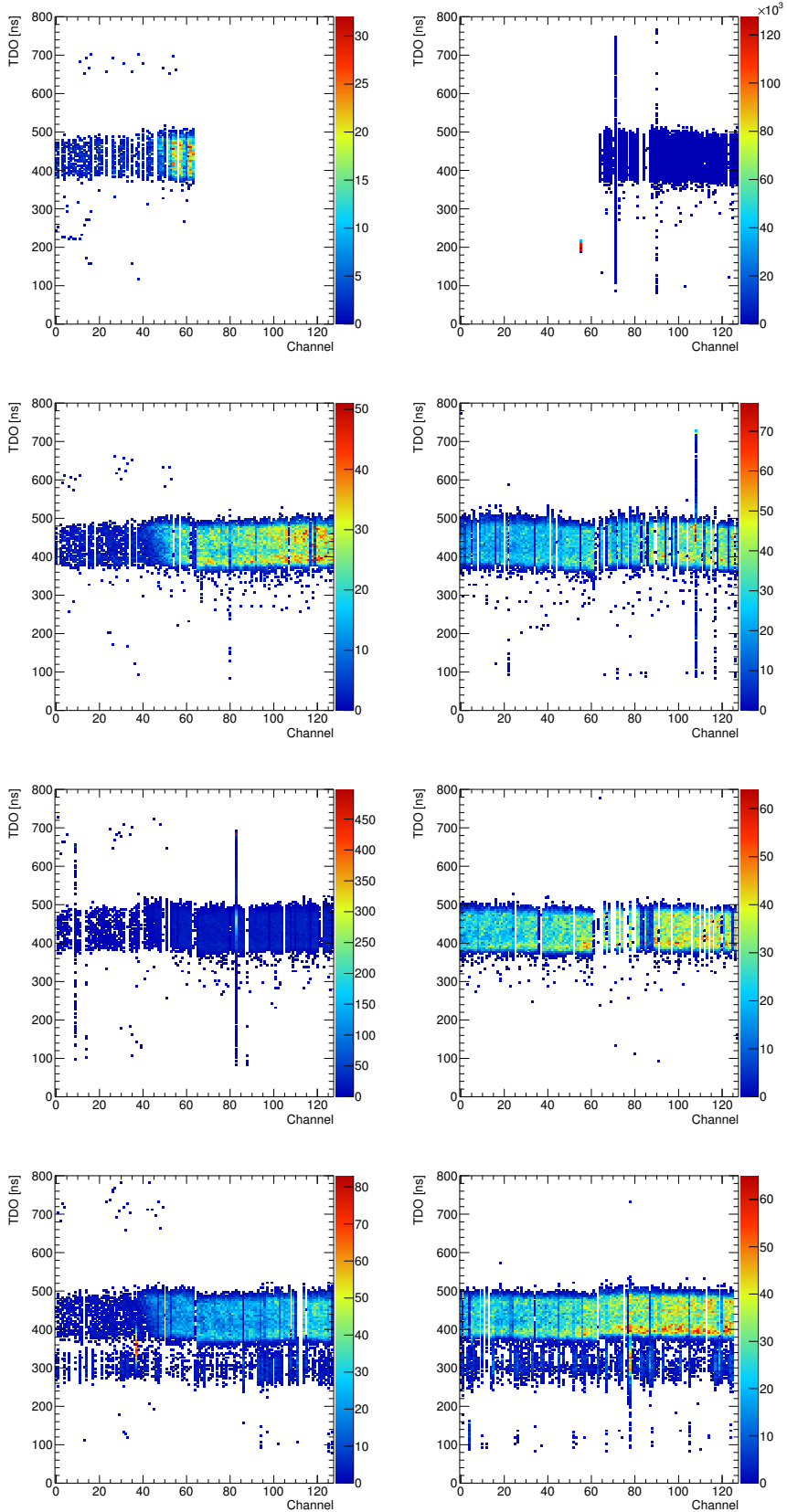


Figure 2: TDO values of each channel in Run 8013. This figure is analogous to Fig. 10 of [1].

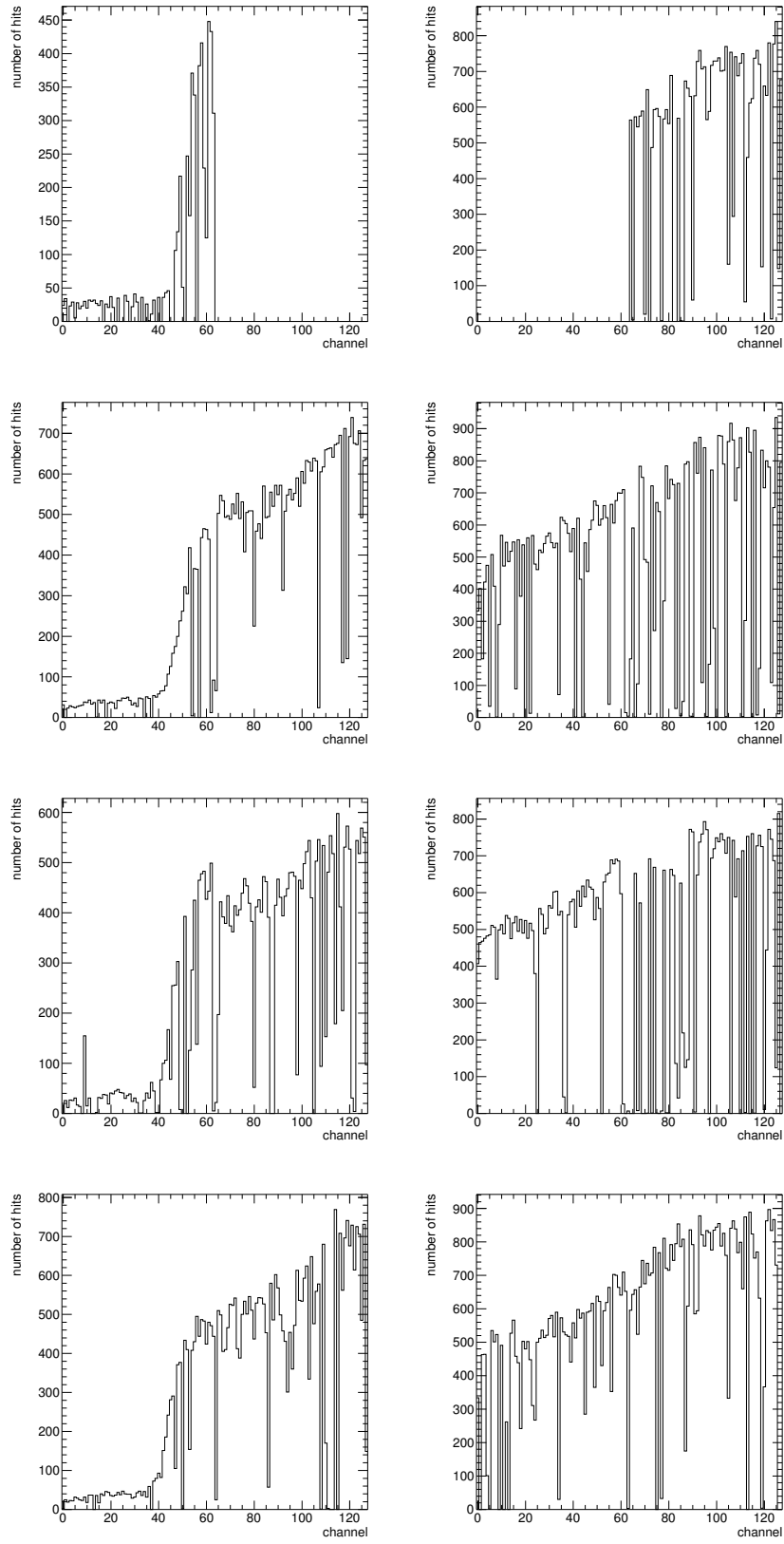


Figure 3: Channel occupancy for chambers T1-T8 in Run 8013. This figure is analogous to Fig. 11(a) of [1].

Not reviewed, for internal circulation only

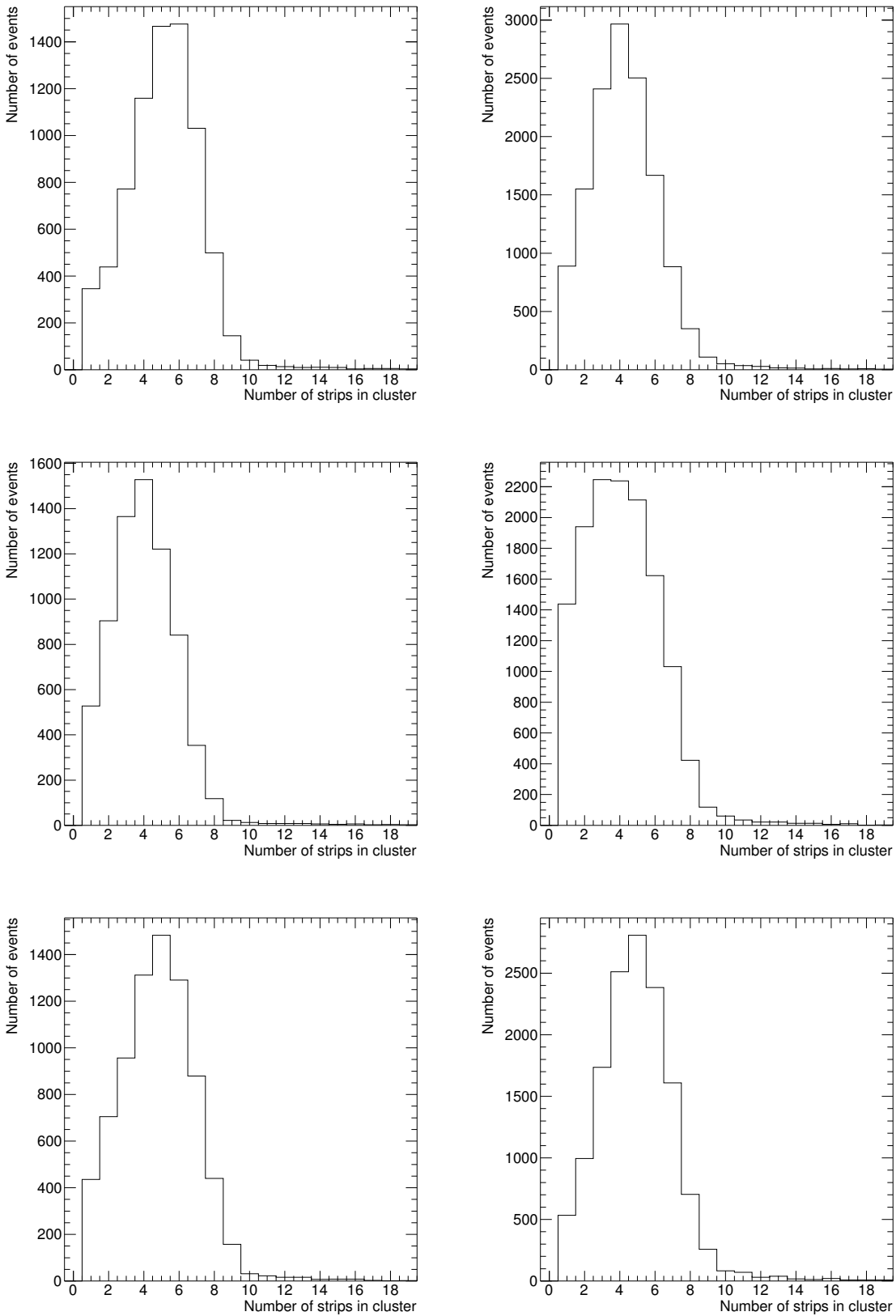


Figure 4: Hit multiplicity of clusters reconstructed in chambers T3-T8.

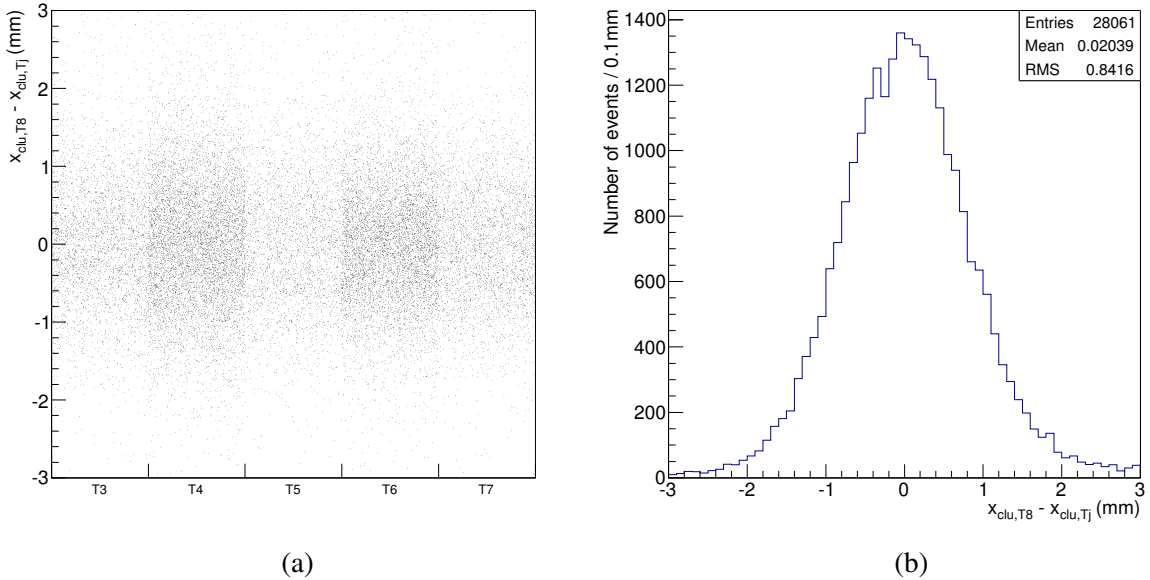


Figure 5: Distributions of (a)  $x_{\text{clu}}^{T8} - x_{\text{clu}}^{Tj}$  for  $j \in [3, 7]$  after alignment; (b) the projection of (a) on its vertical axis.

$x_{\text{clu}}^{Tj}$ , with  $j \in [3, 7]$ . We then fit these distributions with a Gaussian function and add to  $x_{\text{clu}}^{Tj}$  the  $x_{\text{clu}}^{T8} - x_{\text{clu}}^{Tj}$  value of the fitted peak.

For each chamber, we then construct the distribution  $x_{\text{clu}}^{Tj} - x_{\text{tpc}}^{Tj}$  for each chamber  $Tj$ . We add an *ad hoc* offset  $t_0(j)$  to the TDO values of each chamber so that each  $x_{\text{clu}}^{Tj} - x_{\text{tpc}}^{Tj}$  distribution peaks at  $x_{\text{clu}}^{Tj} - x_{\text{tpc}}^{Tj} = 0$ .

Figure 5 shows the  $x_{\text{clu}}^{T8} - x_{\text{clu}}^{Tj}$  with  $j \in [3, 7]$  after the alignment. The projection of this plot on its vertical axis shows that the centroid resolution is 0.65 mm. Fig. 6 shows the distribution  $x_{\text{clu}}^{Tj} - x_{\text{tpc}}^{Tj}$  for  $j \in [3, 8]$ . The projection on the vertical axis shows that the RMS deviation is 1.7 mm, in nice agreement with our finding in Ref. [1] that ruffled many feathers.

Figure 7 shows distribution of  $x_{\text{clu}}^{Tk} - x_{\text{clu}}^{Tj}$  and of  $x_{\text{tpc}}^{Tk} - x_{\text{tpc}}^{Tj}$ , with  $j \neq k$  and  $j, k \in [3, 8]$  in each event. The  $\mu$ TPC method is used with  $\geq 3$  strip clusters. One sees that the resolution of the centroid method is 0.64 mm whereas that of the  $\mu$ TPC methods is 1.34 mm when using all and not just 10% of the events as in Ref. [2]. If combining the two methods with their measured resolution, the  $\mu$ TPC method does not improve the spatial resolution of the centroid.

## 4 One attempt to improve the spatial resolution

Figure 8 shows the RMS deviation of the  $x_{\text{clu}}^{Tk} - x_{\text{clu}}^{Tj}$  and  $x_{\text{tpc}}^{Tk} - x_{\text{tpc}}^{Tj}$  distributions with  $j \neq k$  and  $j, k \in [3, 8]$  as a function of  $n$ , the cluster multiplicity (for each event, we compare clusters in different chambers but with the same multiplicity). The centroid resolution is fitted by the function  $\sigma(n) = 0.74 + 1.1 \exp(-0.57 n)$  (mm), which corresponds to a centroid spatial resolution (in mm again) of

$$\sigma_{\text{bar}}(n) = 0.52 + 0.78 \exp(-0.57 n). \quad (1)$$

The  $\mu$ TPC resolution is fitted by the function  $\sigma(n) = 1.5 + 37.2 \exp(-1.13 n)$  (mm) which corresponds to the  $x_{\text{tpc}}$  resolution  $\sigma_{\text{tpc}}(n) = 1.1 + 26.3 \exp(-1.13 n)$  (mm). The  $x_{\text{tpc}}$  resolution is generally a factor of two worse than that of the centroid.

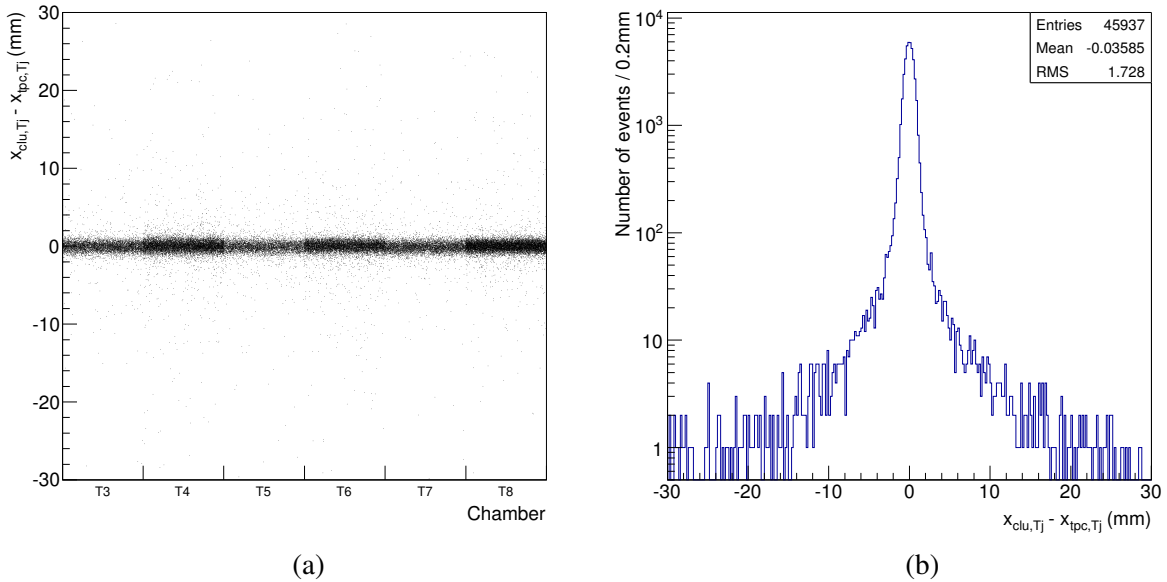


Figure 6: Distributions of  $x_{\text{clu}}^{T_j} - x_{\text{tpc}}^{T_j}$  for  $j \in [3, 7]$  after alignment, when requiring  $|x_{\text{clu}}^{T_8} - x_{\text{clu}}^{T_j}| < 3$  mm and at least 3 strips in cluster. Right: the projection of the plot on its vertical axis.

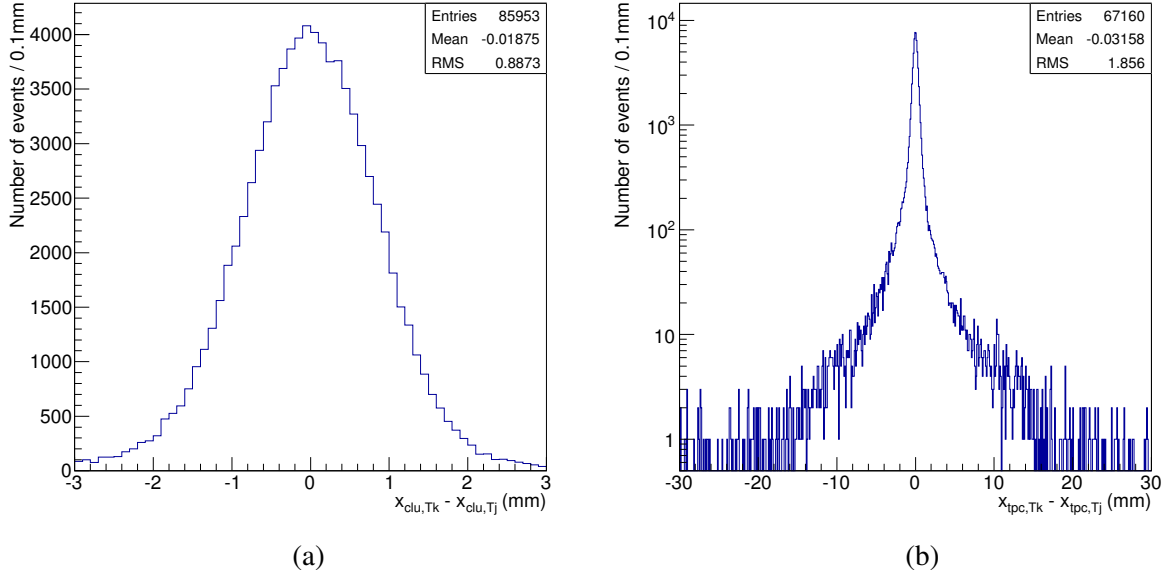


Figure 7: Distributions of (a)  $x_{\text{clu}}^{T_k} - x_{\text{clu}}^{T_j}$  and (b)  $x_{\text{tpc}}^{T_k} - x_{\text{tpc}}^{T_j}$  (see text).

The distribution of  $x_{\text{tpc}}^{T_k} - x_{\text{tpc}}^{T_j}$  for  $j \neq k$  and  $j, k \in [3, 8]$  using  $\geq 3$ -strip clusters is shown in Fig. 9. The distribution is reasonably fitted with four Gaussian functions. The fit result from  $-10$  to  $10$  mm (96% of all events) is shown in Table 2. One notes that for  $\simeq 57\%$  of the events the resolution of  $x_{\text{tpc}}$  is significantly better than that of  $x_{\text{clu}}$ . However, one cannot make use of it when combining the two methods because the overall  $x_{\text{tpc}}$  resolution is 1.34 mm. In order to make a proper use of the often better resolution of the  $\mu$ TPC mode one has to find an additional criterium to determine the accuracy of  $x_{\text{tpc}}$  on an event-by-event basis.

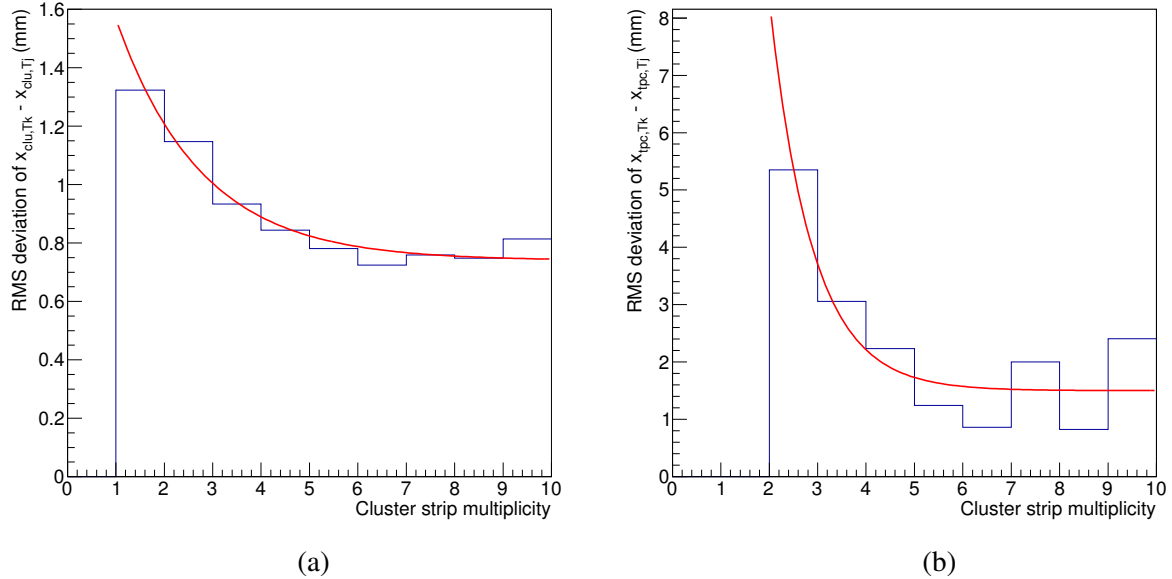


Figure 8: Plot of the RMS deviation of the distribution (a)  $x_{\text{clu}}^{Tk} - x_{\text{clu}}^{Tj}$  and (b)  $x_{\text{tpc}}^{Tk} - x_{\text{tpc}}^{Tj}$  with  $j \neq k$  and  $j, k \in [3, 8]$ , using clusters with the same multiplicity  $n$ , as a function of  $n$ .

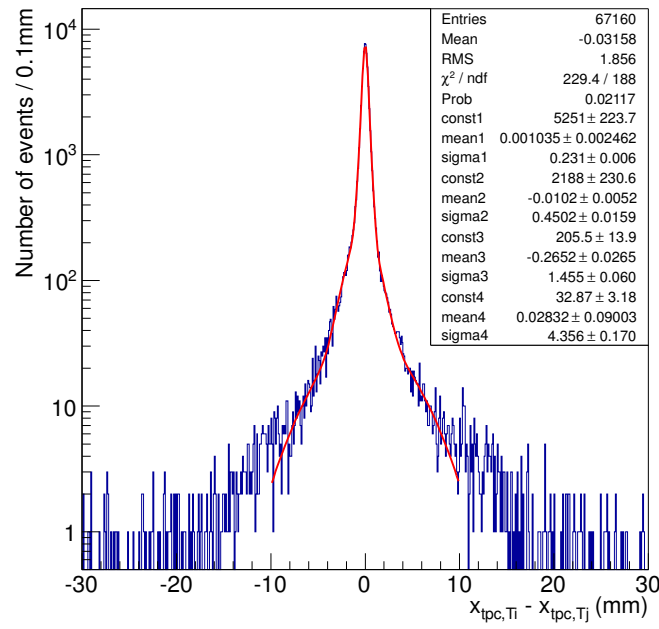


Figure 9: Distribution of  $x_{\text{tpc}}^{Tk} - x_{\text{tpc}}^{Tj}$  for  $j \neq k$  and  $j, k \in [3, 8]$  using  $\geq 3$ -strip clusters. The line is a fit with four Gaussian functions.

Not reviewed, for internal circulation only

Table 2: Result of the fit to Fig. 9.

$\sigma_{\text{fit}}$ (mm)	No. of events	$\sigma_{\text{tpc}}$ (mm)	fraction of events (%)
0.29	37959	0.20	57.2
0.52	18222	0.37	27.5
1.66	7036	1.17	10.6
4.76	3078	3.37	4.7

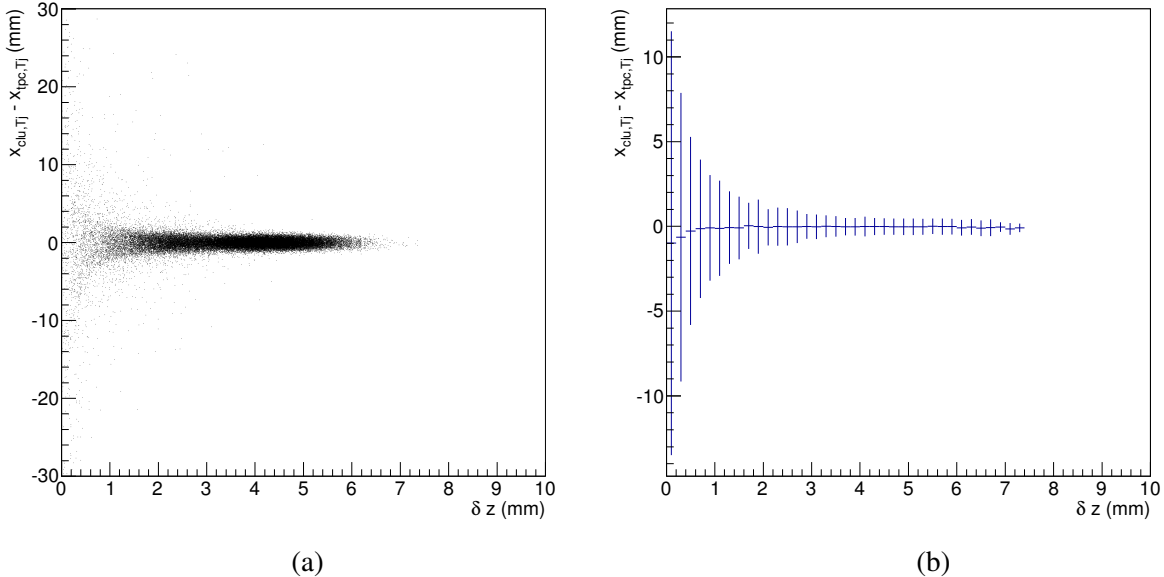


Figure 10: Distribution (a) of  $x_{\text{clu}}^{Tj} - x_{\text{tpc}}^{Tj}$  with  $j \in [3, 8]$  as a function of  $\delta z$  (see text). The profile of this distribution (b) is also shown.

The normalized  $\chi^2$  of the  $\mu$ TPC fit is the first variable we thought of. Ironically, the  $x_{\text{tpc}}$  resolution improves slightly at very large  $\chi^2/\text{NDOF}$  values. The second attempt is more successful and we describe it below.

We choose the variable  $\delta z = |z(x_l) - z(x_f)|$ , where  $z$  is the  $z$  coordinate returned by the  $\mu$ TPC fit and  $x_f$  and  $x_l$  are the  $x$  coordinates of the first and last strips used in the fit. If  $\delta z$  is much smaller than 5 mm, it signals that either only a lopsided fraction of the 8 strips (expected for a 30° track) is detected or that some erroneous TDO value is biasing the fit. Figure 10 shows the  $x_{\text{clu}} - x_{\text{tpc}}$  distribution as a function of this variable for  $\geq 3$ -strip clusters. One notes that for  $\delta z \geq 3$  mm the RMS deviation of  $x_{\text{clu}}^{Tj} - x_{\text{tpc}}^{Tj}$  is comparable with if not smaller than the  $x_{\text{clu}}$  uncertainty.

Figure 11 shows the distribution of  $x_{\text{clu}}^{Ti} - x_{\text{clu}}^{Tj}$  with  $i \neq j$  and  $i, j \in [3, 8]$ . We use events that also have a  $\mu$ TPC measurement ( $\geq 3$ -strip clusters) and we plot the difference as a function of  $\delta z(Ti)$ . The RMS deviation of this plot is properly fitted by the function  $\sigma_1(\delta z) = 0.73 + 0.435 \exp(-0.58 \delta z)$ .

This resolution can also be written as  $\sigma_1^2 = \sigma_{\text{bar}}^2 + \sigma_{\text{bar}}^2 f(\delta z)^2$ , where  $\sigma_{\text{bar}} = 0.83 / \sqrt{2}$  is the barycenter resolution averaged over all cluster multiplicity and  $f(\delta z)$  is a function describing the  $\sigma_{\text{bar}}$  dependence on  $\delta z$ . It follows that  $f(\delta z)^2 = 2 (\sigma_1 / 0.85)^2 - 1$ , and

$$\sigma_{\text{bar}}^2 = (0.52 + 0.78 \exp(-n 0.57))^2 (2.0 (0.88 + 0.52 \exp(-0.58 \delta z)) - 1.0). \quad (2)$$

Figure 12 shows the RMS deviation of the difference  $x_{\text{clu}} - x_{\text{tpc}}$  in Fig. 10 after removing the  $\sigma_{\text{bar}}$

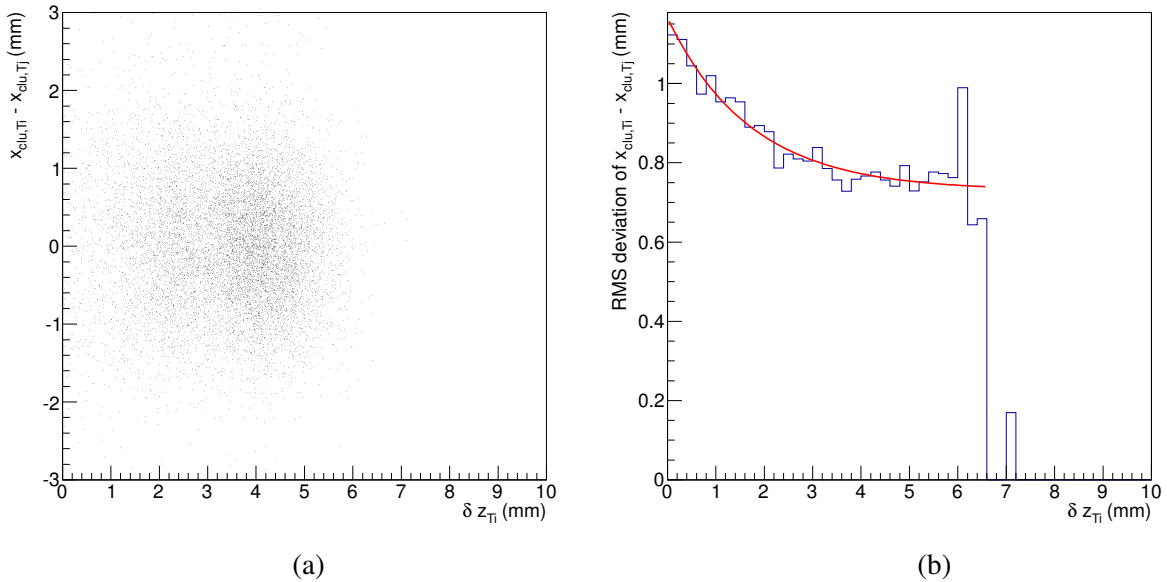


Figure 11: Distribution (a) of  $x_{\text{clu}}^{Ti} - x_{\text{clu}}^{Tj}$  with  $i \neq j$  and  $i, j \in [3, 8]$  as a function of  $\delta z(Ti)$  (see text). The RMS of this distribution (b) is also shown as a function of  $\delta z(Ti)$ .

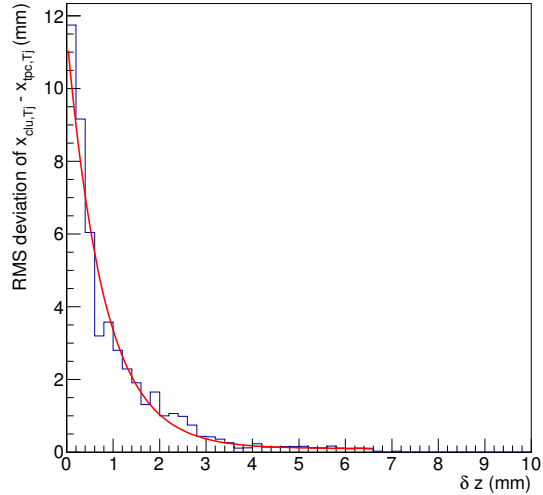


Figure 12: RMS deviations of  $x_{\text{clu}}^{Tj} - x_{\text{tpc}}^{Tj}$  with  $j \in [3, 8]$  as a function of  $\delta z$ , after removing the centroid resolution according to Eqn. 2.

contribution in Eqn. 2<sup>1</sup>. The  $x_{\text{tpc}}$  resolution is well fitted with the function

$$\sigma_{\text{tpc}} = 0.1 + 11.4 \exp(-1.25 \delta z) \text{ (mm)}. \quad (3)$$

We call  $x_{\text{pos}} = (x_{\text{clu}}/\sigma_{\text{clu}}^2 + x_{\text{tpc}}/\sigma_{\text{tpc}}^2)/(\sigma_{\text{clu}}^{-2} + \sigma_{\text{tpc}}^{-2})$  the spatial coordinate obtained combining  $x_{\text{clu}}$  and  $x_{\text{tpc}}$  using the weights in Eqn. 2 and 3, respectively. As shown by Fig. 13, the spatial resolution of  $x_{\text{pos}}$  is 0.5 mm, to be compared to a resolution of 0.64 mm for  $x_{\text{clu}}$  and 1.34 mm for  $x_{\text{tpc}}$ . The distribution is

<sup>1</sup>We have verified that  $\sigma_{\text{tpc}}(\delta z)$  does not depend on the cluster multiplicity.

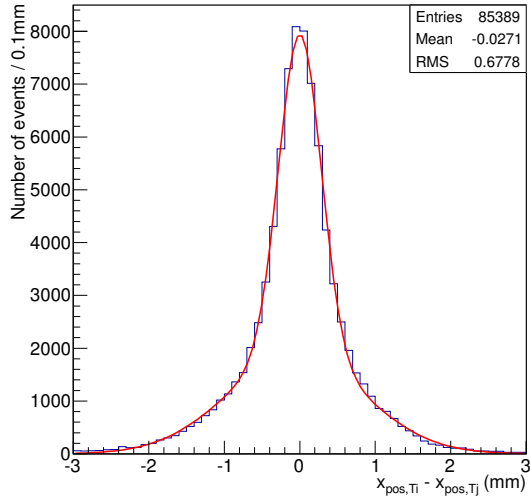


Figure 13: Distribution of  $x_{\text{pos}}^{Ti} - x_{\text{pos}}^{Tj}$  with  $i \neq j$  and  $i, j \in [3, 8]$ . The red line is the fit in Table 3.

Table 3: Result of the fit to Fig. 9.

$\sigma_{\text{fit}}$ (mm)	No. of events	$\sigma_{\text{pos}}$ (mm)	fraction of events (%)
0.28	42939	0.20	50.6
0.91	41581	0.64	49.4

well fitted by two Gaussian functions whose parameters are listed in Table 3. One sees that in 50% of the events the resolution is dominated by the  $\mu$ TPC method which has a resolution of 0.2 mm. The accuracy of spatial position of the remaining 50% of the events is that of the centroid. In conclusion, in spite of the fact that  $x_{\text{tpc}}$  may attain a 0.1 mm resolution in a small fraction of events, the spatial resolution in the full 2012-test-beam dataset is 0.5 mm. In the test-beam data, the VMM1 settings (thresholds too low and VMM1 reset too early) were not optimal and resulted in a significant number of dead channels. These problems did not affect the cosmic data studied in Ref. [1]. The fact that the  $\mu$ TPC resolution in the latter data is in the same ballpark as the test-beam data suggests that the poor resolution is not the result of the test-beam-settings shortcomings. One might expect the centroid resolution to be significantly better if it were possible to lower the VMM thresholds without killing channels. As shown in [1], the  $\mu$ TPC resolution is due to the uncertainty of the VMM peaktiming in determining the electron drift time [1], and will hardly be improved.

## 5 Comparison with ATL-COM-MUON-2015-001

We start by listing all differences between our requirements and those of Ref. [4]:

- We use only strips with PDO values between 360 and 520 ns. As shown by a comparison of Fig. 3 in this note to Fig. 2 of [4], this additional requirement gets rid of a number of hot channels.
- We correct PDO and TDO values for the VMM leakage.

Fig. 7 of this note shows distributions of  $x_{\text{clu}}^{Tk} - x_{\text{clu}}^{Tj}$  and  $x_{\text{tpc}}^{Tk} - x_{\text{tpc}}^{Tj}$ , respectively, for every micromega-pair combination. For 30° tracks, we see no difference in the RMS deviation of a pair as a function of

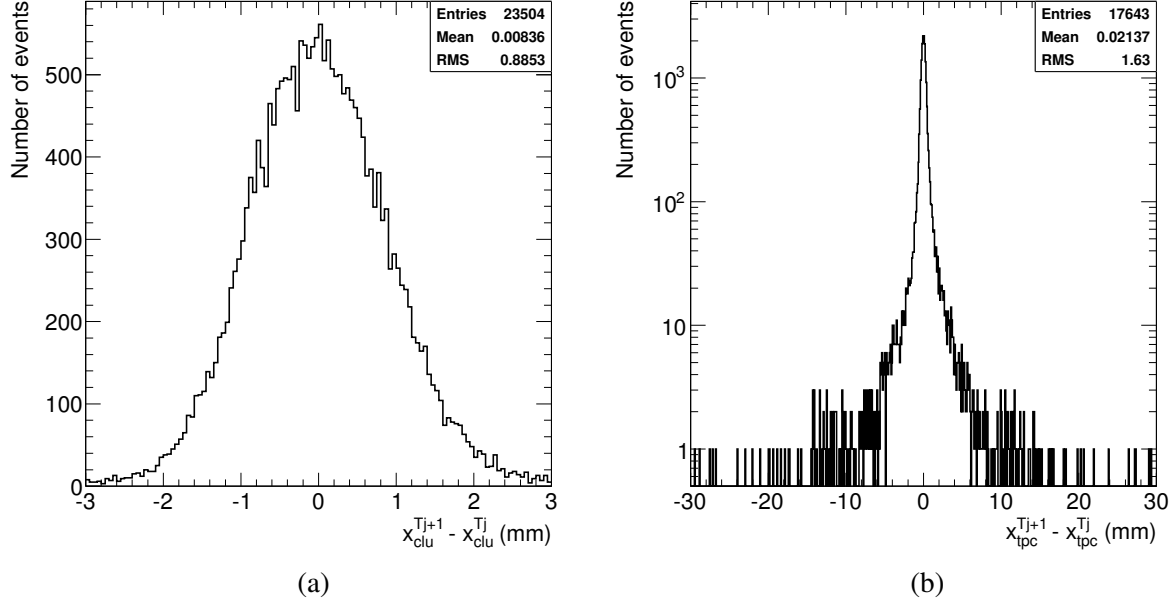


Figure 14: Distributions of (a)  $x_{\text{clu}}^{Tj+1} - x_{\text{clu}}^{Tj}$  and (b)  $x_{\text{tpc}}^{Tj+1} - x_{\text{tpc}}^{Tj}$  with  $j \in [3, 7]$  (see text).

their respective distance along the beamline. However, there is an appreciable difference for  $0^\circ$  tracks. To compare with Ref. [4], we plot again these distributions for  $k = j + 1$  in Fig. 14. From the distribution of the centroid difference one derives a RMS centroid resolution of 0.625 mm, 15% larger than that quoted in Fig. 13 of [4] in a smaller range. The corresponding RMS resolution of  $x_{\text{tpc}}$  over a 6 cm range is 1.15 mm (note that we plot  $x_{\text{tpc}}^{Tk} - x_{\text{tpc}}^{Tj}$  only if the difference of the centroids is smaller than 3 mm). For comparison, in the same range, the RMS uncertainty of  $x_{\text{tpc}}^{T4} - x_{\text{tpc}}^{T3}$  distribution in Fig. 17 of Ref. [4] would be 2.66 mm [7]. We believe that this much worse RMS uncertainty is produced by using strips with illegal TDO values and by fitting strips with a distance larger than 2 mm from the centroid position, but do not investigate this further.

We note that our distribution of the centroid difference uses also clusters with only one strip which are not used in Ref. [4]. As shown by Fig 15, 1-strip clusters are not noise hits, and neglecting them lowers the micromega efficiency of by about 6.5%, somewhat consistent with the reconstruction efficiencies in Table 2 of Ref. [4]. However, their inclusion worsens the centroid spatial resolution.

In Sec. 4, we have determined the uncertainty of  $x_{\text{tpc}}$  on an event-by-event basis by using the variable  $\delta z = |z(x_l) - z(x_f)|$ , where  $z$  is the  $z$  coordinate returned by the  $\mu$ TPC fit and  $x_f$  and  $x_l$  are the  $x$  coordinates of the first and last strips used in the fit. The study in Ref. [4] suggests the alternative use of the errors returned by the  $\mu$ TPC fit. Since this method is much simpler to implement, it is of interest and we verify it. Instead of using an arbitrary error for the PDO values, we tune it using the fit-pull and  $\chi^2$ -probability distributions. While the fit result does not depend on the chosen error, the latter distributions are regularized by using an error of 9 ns (or 0.45 mm) as shown by Fig. 16. We note that the RMS deviation of the pull distribution is 1.01 whereas that of Fig. 9 in Ref. [4] is 1.26.

We use the covariance matrix returned by the fit to calculate the uncertainty  $\delta x_{\text{tpc}}$  of  $x_{\text{tpc}}$ . As shown in Sec. 4, the RMS uncertainty of the centroid  $x_{\text{clu}}$  is a function of the cluster multiplicity  $n$  and is well described by the function  $\delta x_{\text{clu}} = 0.52 + 0.78 \exp(-0.57 n)$  (mm) of Eqn. 1.

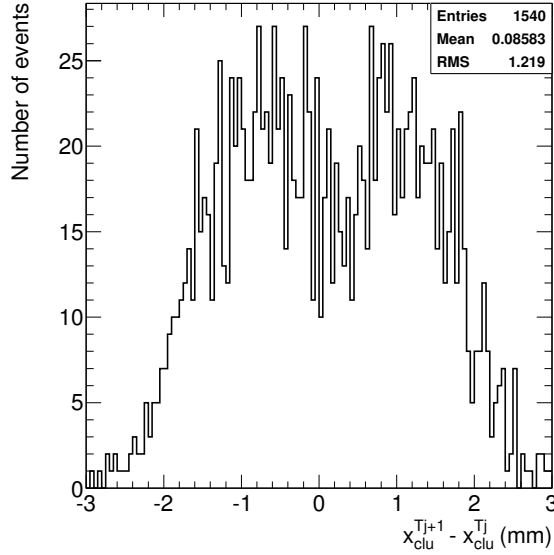


Figure 15: Distribution of  $x_{\text{clu}}^{Tj+1} - x_{\text{clu}}^{Tj}$  with  $j \in [3, 8]$  when at least one of the clusters consists of only one strip (see text).

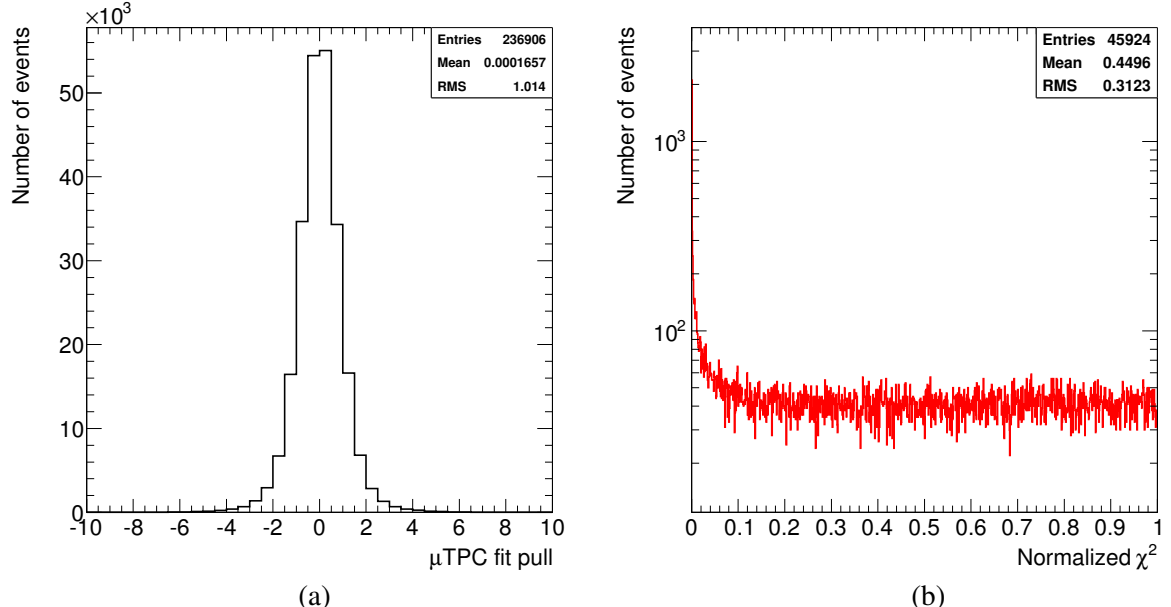


Figure 16: Distributions of (a) the  $\mu$ TPC fit pulls and (b)  $\chi^2$ -probability. Micromegas T3-T8 are used.

We define three pull variables:

$$P^j = (x_{\text{clu}}^{Tj+1} - x_{\text{clu}}^{Tj}) / \sqrt{(\delta x_{\text{clu}}^{Tj+1})^2 + (\delta x_{\text{clu}}^{Tj})^2}, \quad (4)$$

$$Q^j = (x_{\text{clu}}^{Tj} - x_{\text{tpc}}^{Tj}) / \sqrt{(\delta x_{\text{clu}}^{Tj})^2 + (\delta x_{\text{tpc}}^{Tj})^2}, \quad (5)$$

$$S^j = (x_{\text{tpc}}^{Tj+1} - x_{\text{tpc}}^{Tj}) / \sqrt{(\delta x_{\text{tpc}}^{Tj+1})^2 + (\delta x_{\text{tpc}}^{Tj})^2}. \quad (6)$$

Figure 17 shows the distribution of  $P^j$  with  $j \in [3, 7]$ . Figure 18 shows (a) the distribution of  $Q^j$  for  $j \in [3, 8]$ , and (b) the distribution of  $S^j$  for  $j \in [3, 7]$ .

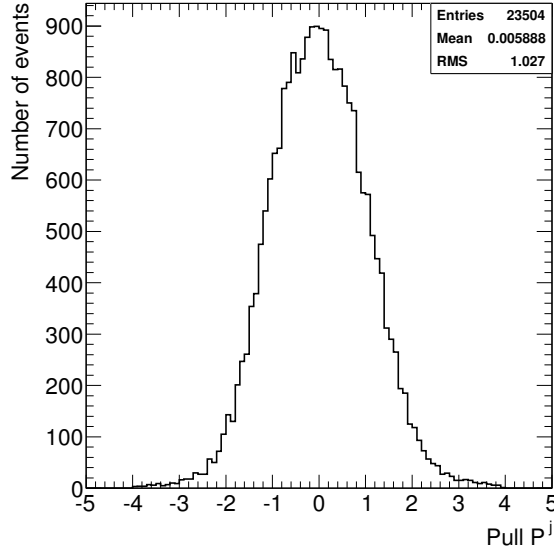


Figure 17: Distribution of the pulls  $P^j$  with  $j \in [3, 7]$  (see text).

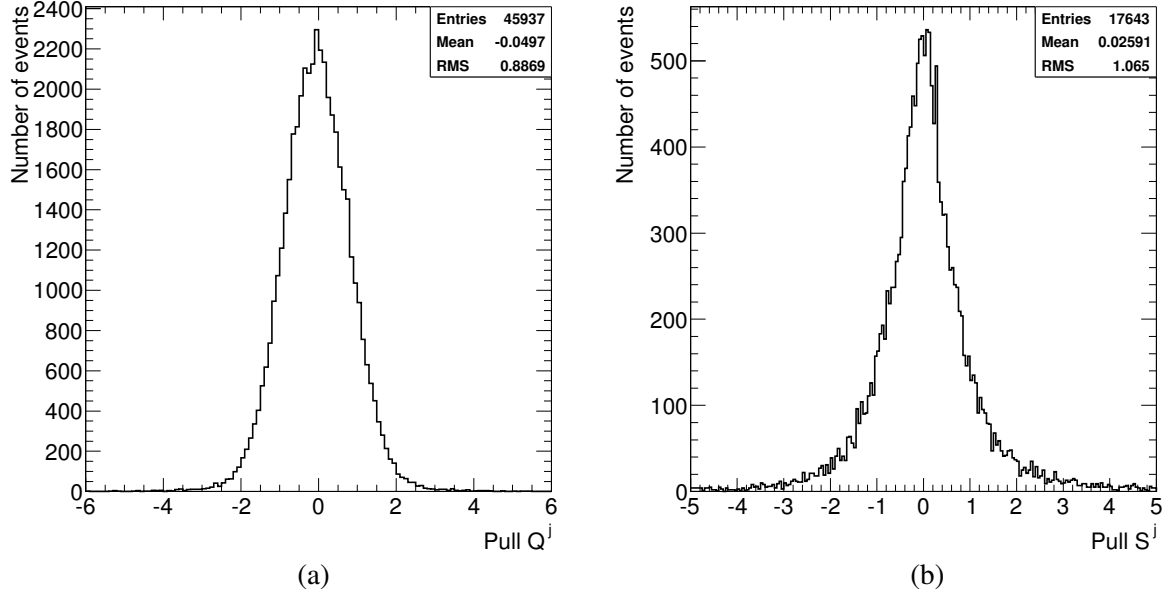


Figure 18: Distributions of the pulls (a)  $Q^j$  with  $j \in [3, 8]$  and (b)  $S^j$  with  $j \in [3, 7]$  (see text).

The RMS deviations of all pull distributions are close to one; however, there are indications that: the RMS uncertainty of  $x_{\text{clu}}$  and  $x_{\text{tpc}}$  are slightly correlated; and the errors  $\delta x_{\text{tpc}}$  are slightly underestimated by the fit and do not follow a proper Gaussian distribution.

All this said, we proceed to next obvious step which is missing in Ref. [4]. In each micromega we re-define the combined spatial coordinate, using  $\mu\text{TPC}$  fit errors instead of  $\delta z$ :

$$x_{\text{pos}} = (x_{\text{clu}}/\delta x_{\text{clu}}^2 + x_{\text{tpc}}/\delta x_{\text{tpc}}^2)/(\delta x_{\text{clu}}^{-2} + \delta x_{\text{tpc}}^{-2}) \quad (7)$$

and its error  $\delta x_{\text{pos}} = 1 / \sqrt{\delta x_{\text{clu}}^{-2} + \delta x_{\text{tpc}}^{-2}}$ . For clusters with multiplicity smaller than three, the centroid is used.

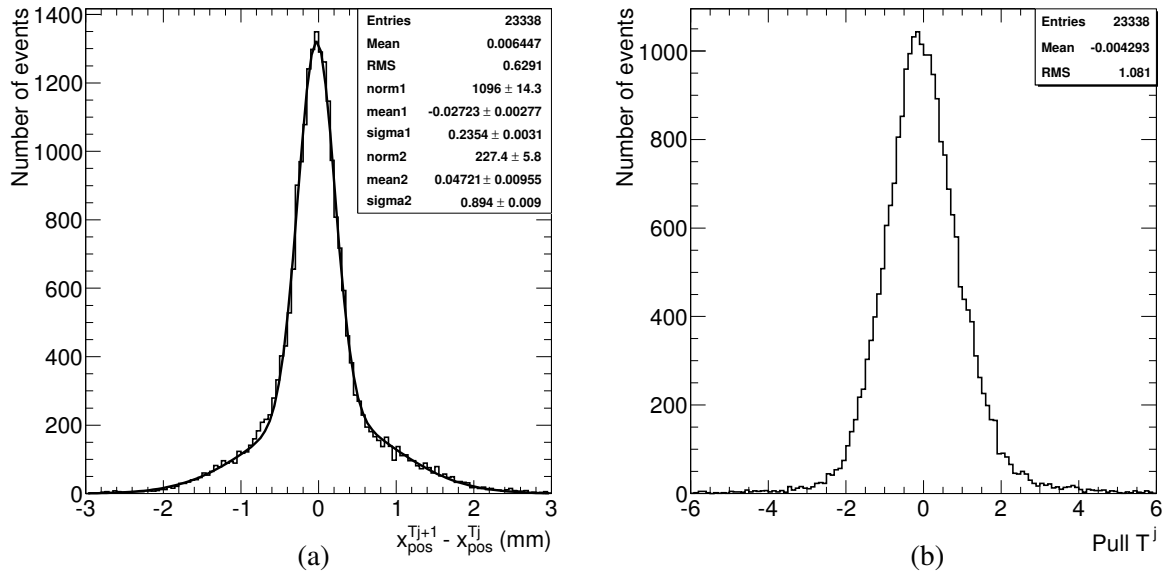


Figure 19: Distributions of (a)  $x_{\text{pos}}^{Tj+1} - x_{\text{pos}}^{Tj}$  and (b) the pulls  $T^j$  with  $j \in [3, 7]$  (see text). The solid line represents a fit with two Gaussian functions.

Figure 19 plots the difference  $x_{\text{pos}}^{Tj+1} - x_{\text{pos}}^{Tj}$  with  $j \in [3, 7]$  and the pull distribution

$$T^j = (x_{\text{pos}}^{Tj+1} - x_{\text{pos}}^{Tj}) / \sqrt{(\delta x_{\text{pos}}^{Tj+1})^2 + (\delta x_{\text{pos}}^{Tj})^2}. \quad (8)$$

The pull distribution shows that the method slightly underestimates the uncertainty  $\delta x_{\text{pos}}$ . The  $x_{\text{pos}}^{Tj+1} - x_{\text{pos}}^{Tj}$  distribution is fairly modeled by two Gaussian functions accounting for 55% of the events with a  $\sigma = 0.25$  mm and 45% of the events with a  $\sigma = 0.8$  mm, which in turn corresponds to spatial resolutions of 0.176 and 0.56 mm, respectively. The overall spatial resolution is of 0.44 mm, consistent with that obtained in Sec. 4. Since the method of using the fit errors is more straightforward, it should be preferred.

For completeness, Figure 20 shows the  $x_{\text{pos}}^{Tj+1} - x_{\text{pos}}^{Tj}$  distributions for events in which both  $x_{\text{pos}}$  coordinates, only one or none are reconstructed using also the  $\mu$ TPC method. Coordinates reconstructed also with the  $\mu$ TPC method have a spatial resolution of 0.37 mm, whereas that of centroids alone (clusters with  $\leq 2$  multiplicity) is 0.94 mm.

## 5.1 Analysis of runs with different angles

We extend our study to runs 8007, 8004, and 8000 in which muons have angle of incidence of 20, 10, and  $0^\circ$ , respectively. With the exception of run 8000, the neighbor-enable feature is not used. Runs 8000 and 8004 have a different trigger timing, and to remove readout noise we use TDO values between 440 and 640 ns. Clusters and centroids are reconstructed as in Sec. 3. The  $\mu$ TPC is applied to  $\geq 3$ -strip clusters, and we only use strips the distance of which from the cluster centroids  $\leq 5, 4, 3$  strips for 30, 20, and  $10^\circ$  angles, respectively.

We follow the procedure outlined in Sec. 3 to align the different micromegas T1–T8 for each run. We do not use the  $\mu$ TPC method for the  $0^\circ$  run. We evaluate the spatial coordinate and its error combining the results of the  $\mu$ TPC and centroid methods as in Eqn. 7. Since the RMS uncertainty of  $x_{\text{clu}}$  flattens out for cluster multiplicities larger than three, we approximate it with the function

$$\delta x_{\text{clu}} = 0.203 \exp(0.0337\theta), \quad (9)$$

where  $\theta$  is the muon angle of incidence <sup>2</sup>.

---

<sup>2</sup> For comparison, for cluster multiplicities smaller than three, the uncertainty is  $\delta x_{\text{clu}} = 0.203 \exp(0.049\theta)$ .

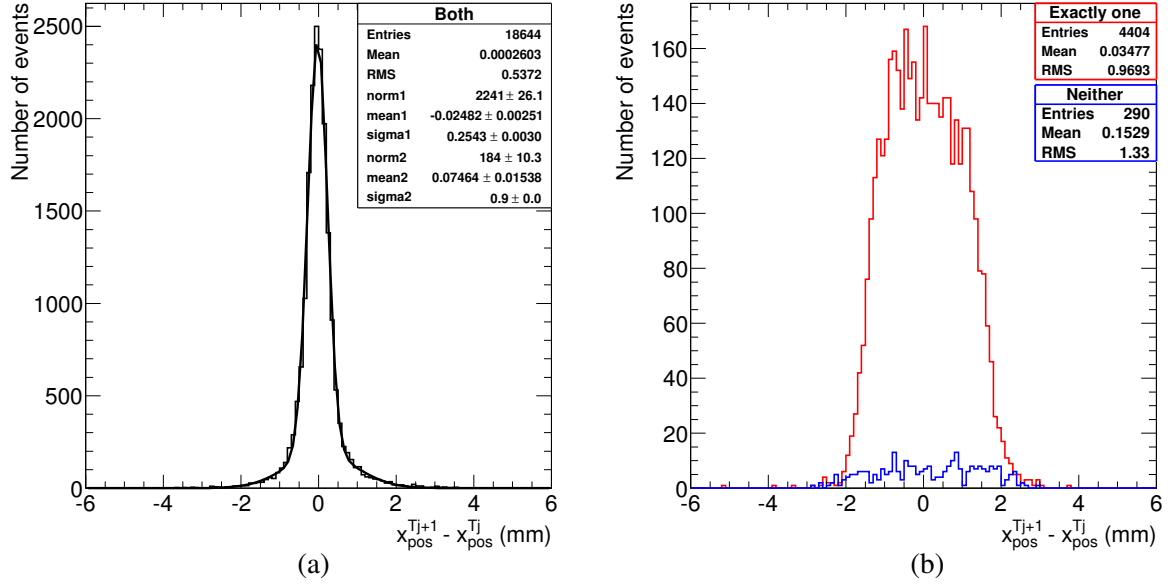


Figure 20: Distributions of  $x_{\text{pos}}^{T_{j+1}} - x_{\text{pos}}^{T_j}$  for events in which (a) both coordinates, and (b) only one (red histogram) or none (blue histogram) are reconstructed using also the  $\mu$ TPC method. The solid line represents a fit with two Gaussian functions.

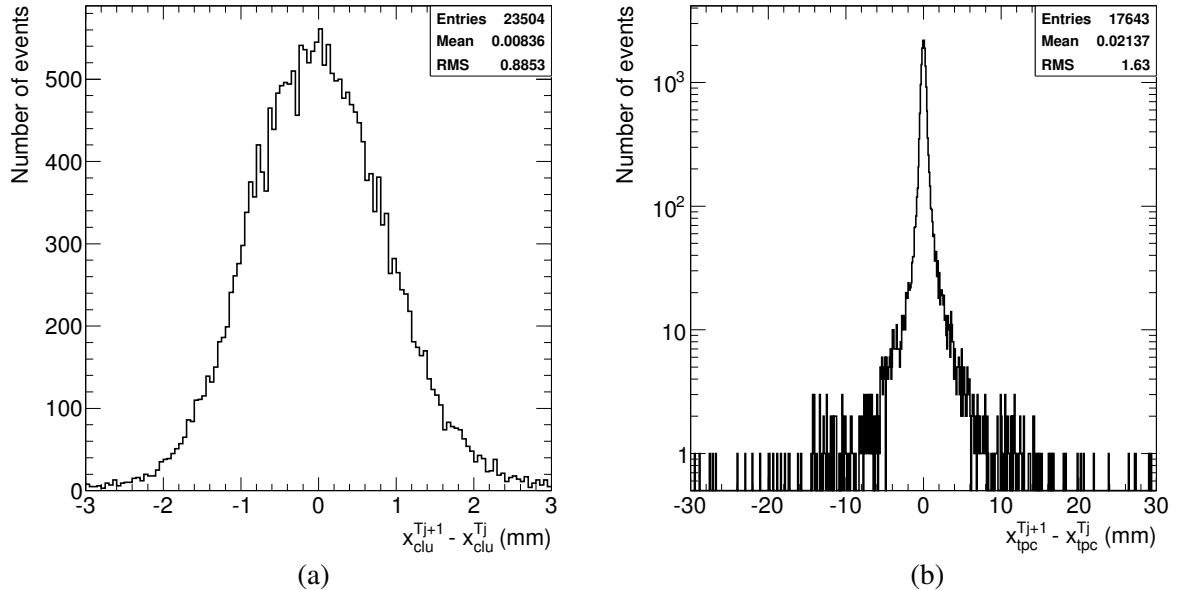


Figure 21: Distributions of (a)  $x_{\text{clu}}^{T_{j+1}} - x_{\text{clu}}^{T_j}$  and (b)  $x_{\text{tpc}}^{T_{j+1}} - x_{\text{tpc}}^{T_j}$  with  $j \in [3, 7]$  (see text) for  $30^\circ$  tracks.

The results for different angles are shown in Figs. 21 to 27<sup>3</sup>. The results are also summarized in Table 4 and Fig. 28.

It is worth mentioning the RMS deviation of the  $x_{\text{clu}}^{T_{j+1}} - x_{\text{clu}}^{T_j}$  distribution for  $0^\circ$  tracks shown in Fig. 24. It is just slightly larger than that in Fig. 14 of Ref. [4] because we also use 1-strip cluster and use all chamber pairs and not just the best one. However, by fitting the histogram with two Gaussian

<sup>3</sup> Figure 25 is slightly different from Fig. 19 because the centroid uncertainty is calculated according to Eqn. 9 instead of Eqn. 1.

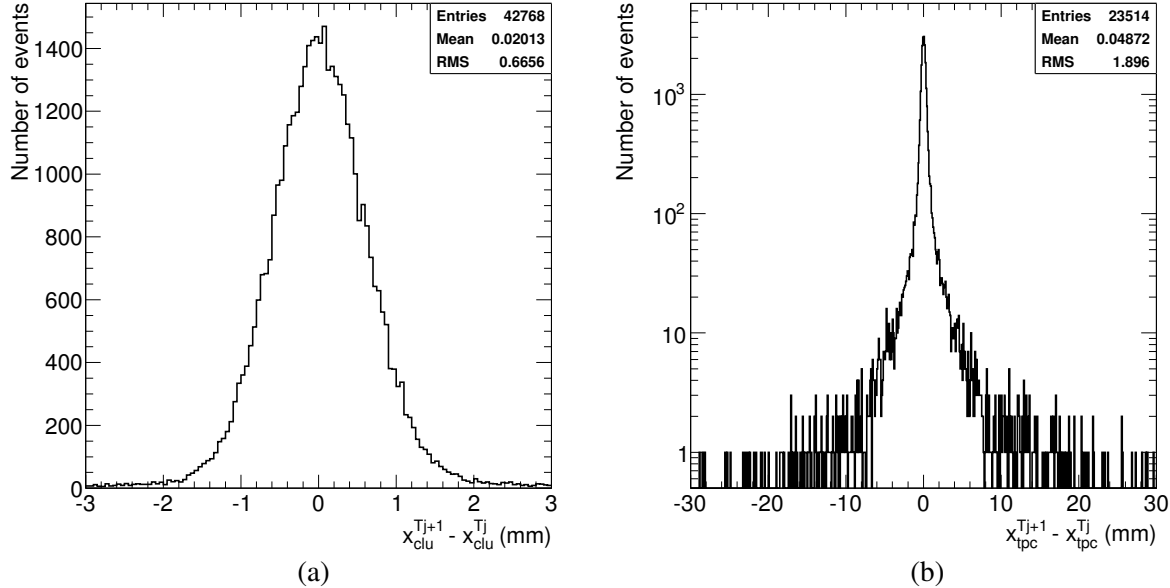


Figure 22: Distributions of (a)  $x_{\text{clu}}^{Tj+1} - x_{\text{clu}}^{Tj}$  and (b)  $x_{\text{tpc}}^{Tj+1} - x_{\text{tpc}}^{Tj}$  with  $j \in [3, 7]$  (see text) for 20° tracks.

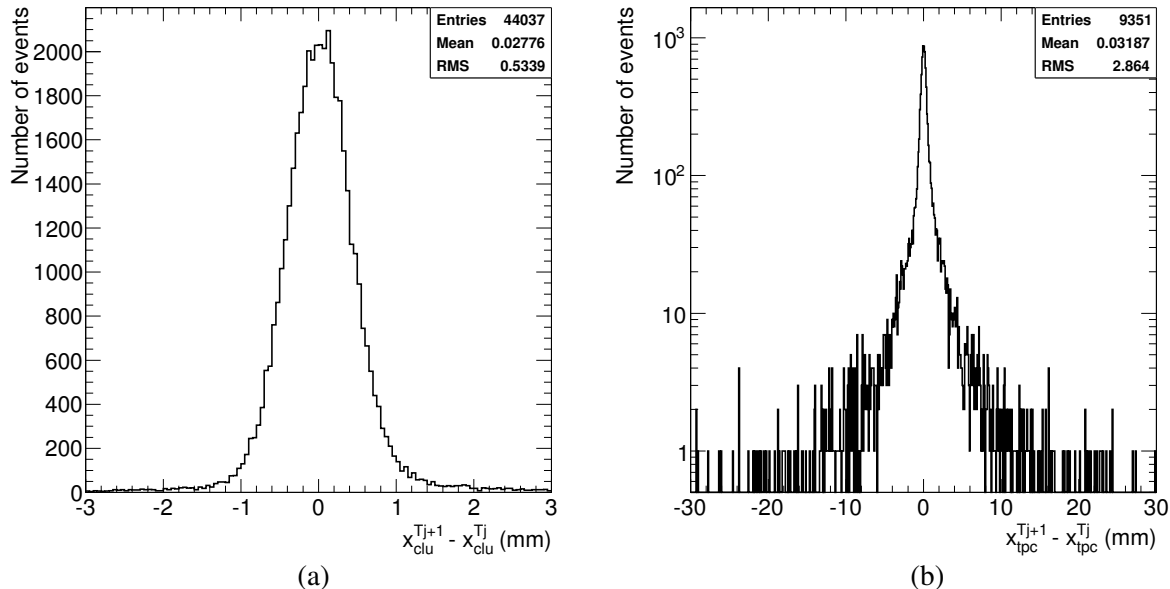


Figure 23: Distributions of (a)  $x_{\text{clu}}^{Tj+1} - x_{\text{clu}}^{Tj}$  and (b)  $x_{\text{tpc}}^{Tj+1} - x_{\text{tpc}}^{Tj}$  with  $j \in [3, 7]$  (see text) for 10° tracks.

functions and using the one with the smaller width, the centroid resolution in Ref. [4] is quoted as 0.07 mm. In conclusion, the spatial resolution of the micromega coordinate measured using the centroid method combined, when possible, with the  $\mu$ TPC method remains 4.5 times larger than that obtained using APV25 electronics and shown in the NSW TDR [3].

## Acknowledgements

We thank the other members of the ATLAS New Small Wheel and Micromegas community for organizing and running the testbeam, and for making the data available to us.

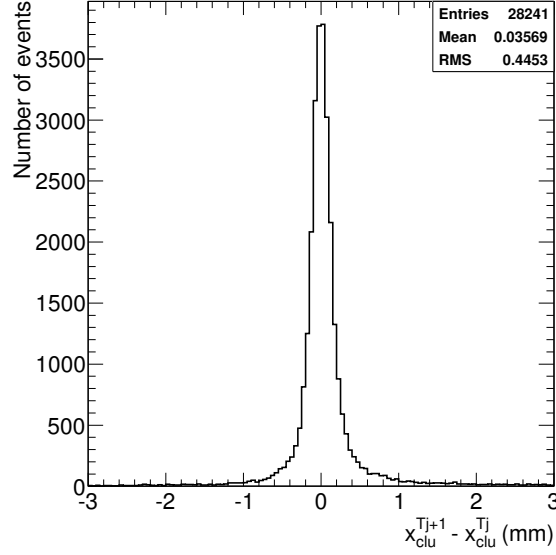


Figure 24: Distribution of  $x_{\text{clu}}^{Tj+1} - x_{\text{clu}}^{Tj}$  with  $j \in [3, 7]$  (see text) for  $0^\circ$  tracks.

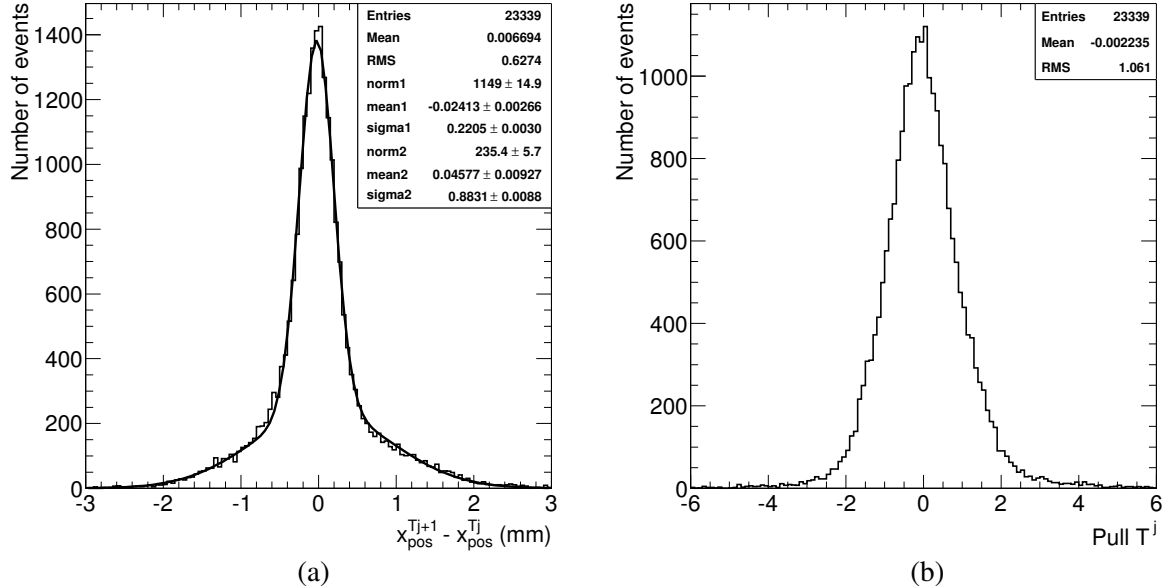


Figure 25: Distributions of (a)  $x_{\text{pos}}^{Tj+1} - x_{\text{pos}}^{Tj}$  and (b) the pulls  $T^j$  with  $j \in [3, 7]$  (see text) for  $30^\circ$  tracks.

## References

- [1] K. DiPetrillo *et al.*, *Test of a resistive micromega v3.0 prototype with VMM1 readout using  $\geq 0.8 \text{ GeV}/c^2$  cosmic muons*, ATL-COM-MUON-2014-038.
- [2] T. Alexopoulos *et al.*, *Performance of the first version of VMM front-end ASIC with resistive micromega detectors*, ATL-UPGRADE-PUB-2014-001.
- [3] ATLAS New Small Wheel Technical Design Report, ATL-TDR-020, CERN-LHCC-2013-006.
- [4] C. Bini *et al.*, ATL-COM-MUON-2015-001.
- [5] G. Iakovidis, /afs/cern.ch/work/g/giakov/public/VMM1\_data, or via ssh (CERN lxplus account) at pcmmdata.cern.ch:/home/data/2012/vmmcdcs/TestBeam\_12\_2012/.

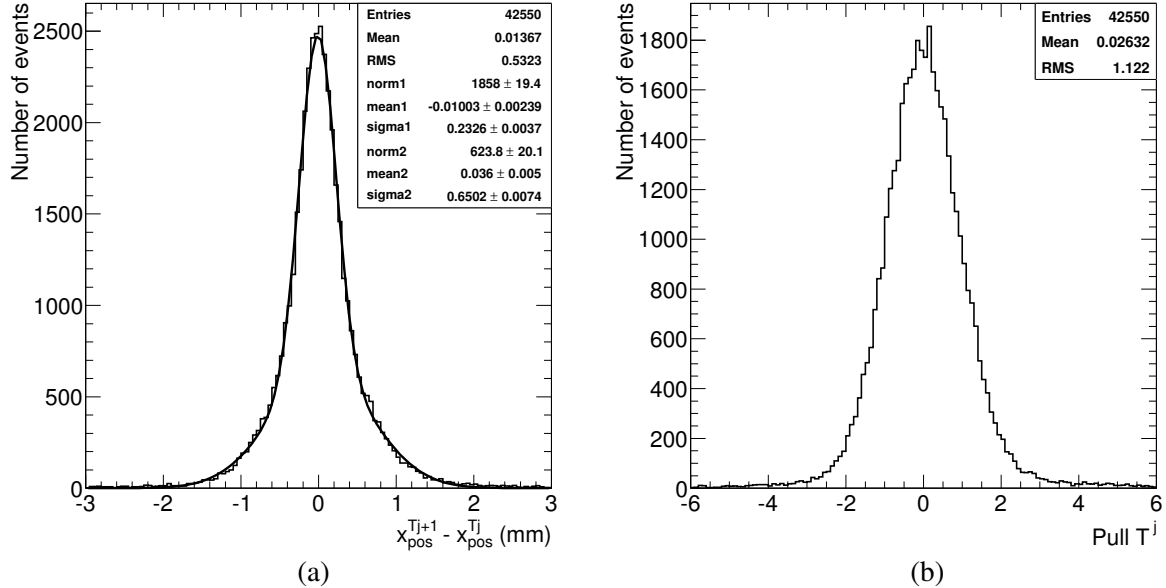


Figure 26: Distributions of (a)  $x_{\text{pos}}^{T_{j+1}} - x_{\text{pos}}^{T_j}$  and (b) the pulls  $T^j$  with  $j \in [3, 7]$  (see text) for  $20^\circ$  tracks.

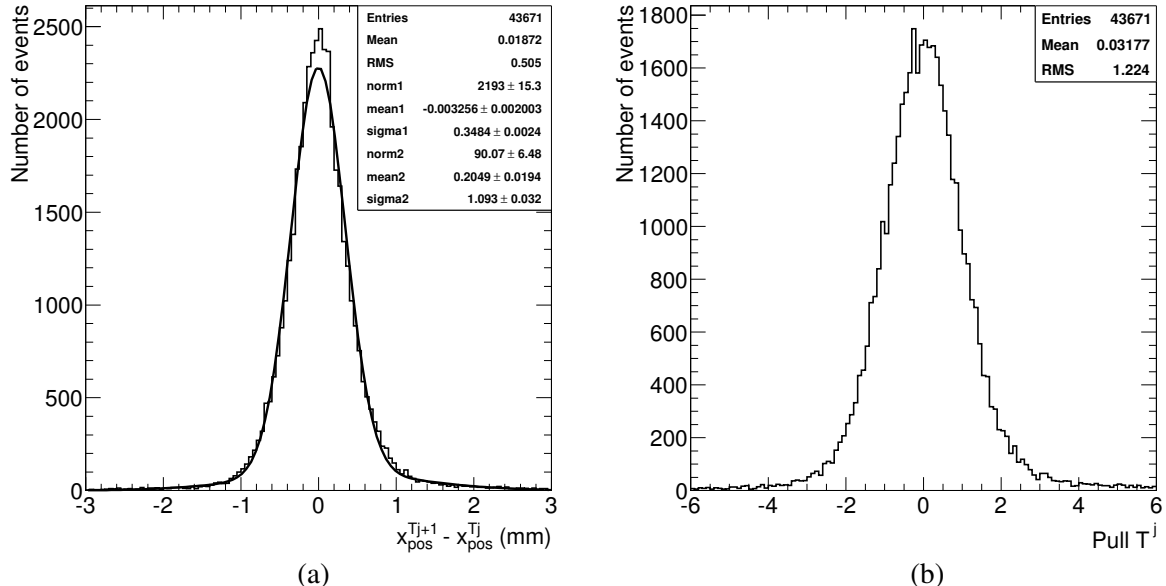


Figure 27: Distributions of (a)  $x_{\text{pos}}^{T_{j+1}} - x_{\text{pos}}^{T_j}$  and (b) the pulls  $T^j$  with  $j \in [3, 7]$  (see text) for  $10^\circ$  tracks.

[6] J. Connors *et al.*, ATL-COM-UPGRADE-2013-034.

[7] M. Vanadia, private communication.

Table 4: RMS uncertainties of various spatial-resolution-related quantities for different track angles and using all pairs of adjacent micromegas from T3 to T8. We define  $\Delta X^j$  as the RMS deviation of the  $x_{\text{pos}}^{Tj+1} - x_{\text{pos}}^{Tj}$  distribution with  $j \in [3, 7]$ ,  $\Delta X_{\text{clu}}$  as that of the  $x_{\text{clu}}^{Tj+1} - x_{\text{clu}}^{Tj}$  distribution, and  $\Delta X_{\text{tpc}}$  as that of the  $x_{\text{tpc}}^{Tj+1} - x_{\text{tpc}}^{Tj}$  distribution.  $\Delta X^j$  is also split into cases in which both coordinates (a), only one (b) or none (c) are reconstructed using also the  $\mu$ TPC method. The pulls  $T^J$ ,  $P^J$ , and  $S^J$  are defined in Eqn. 8, 4, and 6, respectively.

Variable	$30^\circ$	$20^\circ$	$10^\circ$	$0^\circ$
$\Delta X^j$ (mm)	0.627	0.523	0.505	
Pull $T^J$	1.06	1.12	1.22	
$\Delta X^j$ (a) (mm)	0.532	0.469	0.500	
$\Delta X^j$ (b) (mm)	0.970	0.630	0.510	
$\Delta X^j$ (c) (mm)	1.33	0.763	0.529	
$\Delta X_{\text{clu}}$ (mm)	0.885	0.666	0.534	0.440
Pull $P^J$	1.04	1.08	1.10	0.96
$\Delta X_{\text{tpc}}$ (mm)	1.63	1.90	2.86	
Pull $S^J$	0.90	0.87	0.89	

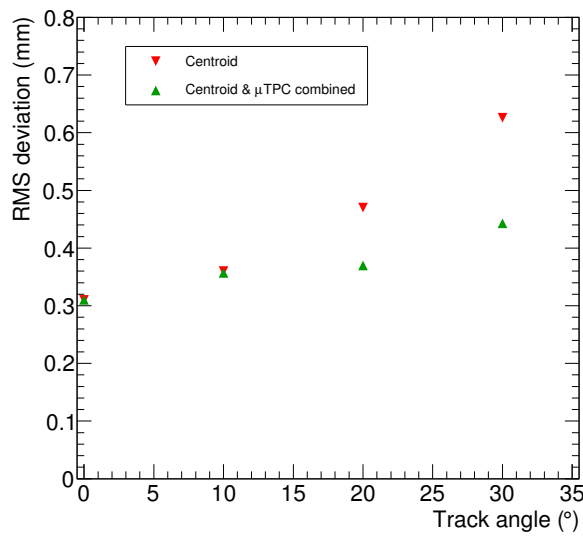


Figure 28: RMS deviations  $\Delta X_{\text{clu}}$  (red points) and  $\Delta X^j$  (green points) divided by  $\sqrt{2}$  as a function of the track angle.